Nano Research

Open Access

Research Article

Dual-interface built-in electric fields induced by sulfidation-driven ordered arrays in MoS_2@C/CoS_x for high-efficiency microwave absorption

Hao Wang[1], Jiarui Zhao[2,3] ✉, and Zhen Wang[4] ✉

[1] State Key Laboratory of Silicate Materials for Architectures, School of Materials Science and Engineering, Wuhan University of Technology, Wuhan 430070, China
[2] School of Mechanical and Precision Instrument Engineering, Xi'an University of Technology, Xi'an 710048, China
[3] State Key Laboratory of Water Engineering Ecology and Environment in Arid Area, Xi'an University of Technology, Xi'an 710048, China
[4] School of Physics and Materials Science, Nanchang University, Nanchang 330096, China

Cite this article: *Nano Research*, **2025**, *18*, 94908070. https://doi.org/10.26599/NR.2025.94908070

ABSTRACT: Rational design of hierarchical structures and a dual-interface built-in electric field (BIEF) are vital for enhancing dielectric loss and directional charge transport in microwave absorption materials (MAMs). Herein, we propose a dual-interface BIEF engineering strategy to construct a multifunctional MoS_2@C/CoS_x composites. Inspired by the spiderweb hunting mechanism, magnetic Co-based Prussian blue (PB) is electro spun with polyacrylonitrile to form Co@CoO/C nanofibers, followed by sulfidation to induce ordered array architectures. The structural evolution enables the formation of heterogeneous MoS_2-CoS_x-C interfaces and modulates the interfacial electric field intensity to enhance dielectric polarization. Density functional theory (DFT) calculations confirm that the work function difference ($\Delta\Phi$) of C/CoS_2/MoS_2 is 6.179 eV, which indicates that the differences $\Delta\Phi$ among MoS_2, CoS_x and C components drive the spontaneous formation of dual-interface BIEF. This facilitates directional charge migration and strong dipolar/interface polarization, significantly improving the microwave attenuation capability. Benefiting from this design, the composite achieves a minimum reflection loss (RL_{min}) of –63.83 dB and a maximum effective absorption bandwidth (EAB_{max}) of 6.96 GHz, covering both C and Ku bands. In addition, the material reveals excellent infrared stealth performance due to its unique spiderweb-inspired ordered array structure. This study provides new insights into interfacial electric field modulation and a generalizable approach for designing multi-band and tunable microwave absorbers with synergistic electromagnetic and thermal stealth functions.

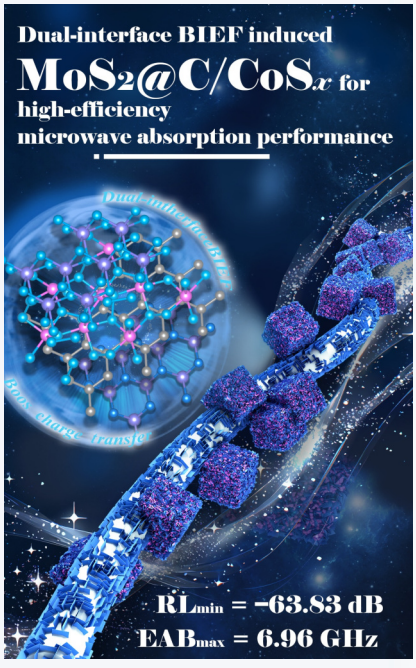

KEYWORDS: Prussian blue (PB), heterostructure, dual-interface built-in electric field (BIEF), dielectric response, microwave absorption (MA) performance

1 Introduction

Currently, the electromagnetic wave (EMW) attenuation capability of microwave absorption materials (MAMs) is largely governed by charge transport behaviors at heterogeneous interfaces [1–3]. Tailoring the nanoscale architecture of multiphase interfaces offers an effective approach to modulating interfacial charge distribution and local electronic states, thereby enhancing interfacial polarization and boosting dielectric loss mechanisms [4]. Consequently, the construction of heterostructures with tunable interfacial electric fields has emerged as a key strategy to enable directional charge migration and improve energy dissipation efficiency.

Heterojunctions formed based on work function differences ($\Delta\Phi$) can induce built-in electric fields (BIEF), which facilitate efficient charge separation and drive their directional movement

Received: August 6, 2025; **Revised:** September 3, 2025
Accepted: September 11, 2025

✉Address correspondence to Zhen Wang, wangzhennpu@163.com; Jiarui Zhao, zhaojrui2233@163.com

across the interface, causing localized interfacial polarization [5, 6]. The incorporation of BIEF enhances dipolar polarization and suppresses energy loss, making it a compelling strategy to improve the microwave absorption (MA) performance of MAMs [7, 8]. The $\Delta\Phi$ between constituent components governs both the directionality and efficiency of interfacial charge transfer, playing a decisive role in modulating charge dynamics. Moreover, the extent of charge polarization determines the strength of interfacial dipole formation, which is critical for efficient energy dissipation. Therefore, strategic design of BIEF at heterointerfaces can induce spatial redistribution of charges and establish interfacial potential gradients, ultimately improving EMW attenuation. For example, Martin C. Koo et al. synthesized a C/TiO_2/NiNW composite by combining MXene (C/TiO_2) with nickel nanowires (NiNWs) via ultrasonic dispersion. The resulting interface between NiNW and TiO_2 formed a strong BIEF that significantly enhanced interfacial charge transport, leading to an increase in a minimum reflection loss (RL_{min}) from −31.93 to −72.77 dB [9]. Similarly, Zhai et al. designed a multidimensional heterostructure of V_2O_3/VO/C@$Ti_3C_2T_x$/TiO_2 via electrostatic self-assembly, enabling concurrent modulation of dielectric properties and BIEF strength. The optimized composite achieved an RL_{min} of −50.10 dB with a maximum effective absorption bandwidth (EAB_{max}) of 6.16 GHz [10]. These examples collectively underscore the effectiveness of BIEF engineering, driven by interfacial charge transfer, to significantly enhance MA properties.

Electrospinning, with its capacity to fabricate interconnected three-dimensional (3D) carbon nanofiber networks, has become a powerful technique for the fabrication of advanced MAMs [11, 12]. Carbon nanofibers (CNFs), owing to their high aspect ratio, excellent electrical conductivity, and low density, have been extensively explored to improve microwave attenuation. Their integration with Prussian blue (PB) has been widely demonstrated as a practical strategy to optimize MA absorption [13, 14]. To illustrate, Wang et al. reported a Co/Mn bimetallic PB carbon fiber composite prepared via electrospinning, which delivered a notable RL_{min} of −58.15 dB at 2.3 mm thickness [15]. Likewise, Han et al. synthesized flexible magnetic CoFe@CNFs by incorporating 1D CNFs with core-shell PB structures through electrospinning and subsequent pyrolysis. Impressively, at a low filler loading of 7.5 wt.%, the composite achieved an RL_{min} of −47.9 dB and an EAB_{max} of 6.5 GHz [16]. However, the collapse of the cubic architecture of PB during high-temperature treatment limits the effectiveness of interfacial polarization and the magneto-dielectric synergism.

Chalcogenide compounds have been widely recognized as promising candidates for BIEF construction [17–19]. Among them, molybdenum disulfide (MoS_2), a representative layered transition metal dichalcogenide, possesses excellent electrical conductivity, chemical stability and substantial dielectric loss, rendering it highly effective in EMW attenuation. For instance, Wang et al. utilized the layer-stacking characteristics of MoS_2 to induce surface charge transfer and localized electric fields, achieving an RL_{min} of −41.9 dB and an EAB_{max} of 3 GHz [20]. Another noteworthy chalcogenide, cobalt sulfide (CoS_x), is a semiconductor with high electron mobility and robust thermal stability [21, 22]. Zhang et al. demonstrated that CoS_2 enriched with sulfur vacancies, combined with CNFs, can serve as effective dielectric polarization centers, yielding an RL_{min} of −59.84 dB and an EAB_{max} of 4.9 GHz [23]. Furthermore, Yang et al. revealed that a CoS_2/Co_3O_4@MoS_2 heterostructure could regulate interfacial BIEF, enabling guided charge transfer and enhancing electrocatalytic activity for the oxygen evolution reaction [24].

In this work, we developed a multifunctional MoS_2@C/CoS_x composites incorporating dual-interface BIEF to achieve broadband MA performance and infrared stealth. The composite is produced by electrospinning followed by thermal annealing to generate a bioinspired spiderweb-like Co@CoO/C framework. A subsequent sulfidation process facilitated the formation of well-ordered heterostructures and modulated the interfacial electric fields between MoS_2, CoS_x and the carbon framework. This sulfidation not merely promoted the formation of heterogeneous interfaces but also induced spontaneous development of dual-interface BIEF at CoS_2/MoS_2 and C/CoS_2/MoS_2 junctions. The synergistic dual-field effect enhanced interfacial polarization and dielectric dissipation, significantly broadening the absorption bandwidth. Consequently, the MoS_2@C/CoS_x composite achieved an RL_{min} of −63.83 dB and an EAB_{max} of 6.96 GHz at a thickness of 2.44 mm. Benefiting from the ordered spiderweb-inspired architecture, the material exhibited full-band absorption across both C and Ku bands, along with excellent infrared stealth capability. This study provides new insights into interface field engineering through dual-interface BIEF construction and offers a promising route toward the design of broadband and high-efficiency MAMs with multifunctional capabilities.

2 Results and discussion

2.1 Morphology and chemical composition of MoS_2@C/CoS_x composites

A dual-interface BIEF MoS_2@C/CoS_x composites with an ordered array structure are successfully fabricated through a multistep process involving electrospinning, carbonization and sulfidation, as illustrated in Fig. 1(a). The structural design is inspired by the natural predatory behavior of spiders. Initially, Co-Prussian blue (CPB) particles are incorporated into polyacrylonitrile (PAN) nanofibers via electrospinning, leading to a biomimetic spiderweb-like structure. In this design, the PAN nanofibers mimic spider silk, while the CPB platonic solid serve as the "prey", forming a CPB@PAN fibrous membranes (inset of Fig. 1(b)). Subsequently, the membranes are subjected to carbonization at 600 °C in a nitrogen atmosphere, causing Co@CoO/C composite. Scanning electron microscopy (SEM) (Fig. 1(b)) revealed that the PAN nanofibers contracted during carbonization, forming curved and entangled structures that resemble spiderwebs. Meanwhile, the CPB "prey" decomposed into cobalt particles with roughened surfaces, which became tightly encapsulated within the carbon nanofiber network. Further transmission electron microscopy (TEM) (Figs. S1(a) and S1(b) in the Electronic Supplementary Material (ESM)) and energy-dispersive X-ray spectroscopy (EDS) analysis (Figs. S1(c) and S1(d) in the ESM) confirmed that these particles mainly consisted of cobalt oxides.

Following sulfidation in the presence of sulfur and molybdenum precursors, partial conversion of Co nanoparticles and CoO into cobalt sulfides (CoS_x) is achieved. By tuning the molybdenum precursor content, heterogeneous interfaces are successfully constructed within the MoS_2@C/CoS_x composites, resulting in an ordered array structure along with a continuous conductive network (Figs. S2–S4 in the ESM). The morphology of the optimized MoS_2@C/CoS_x-1.0 is examined using SEM and TEM

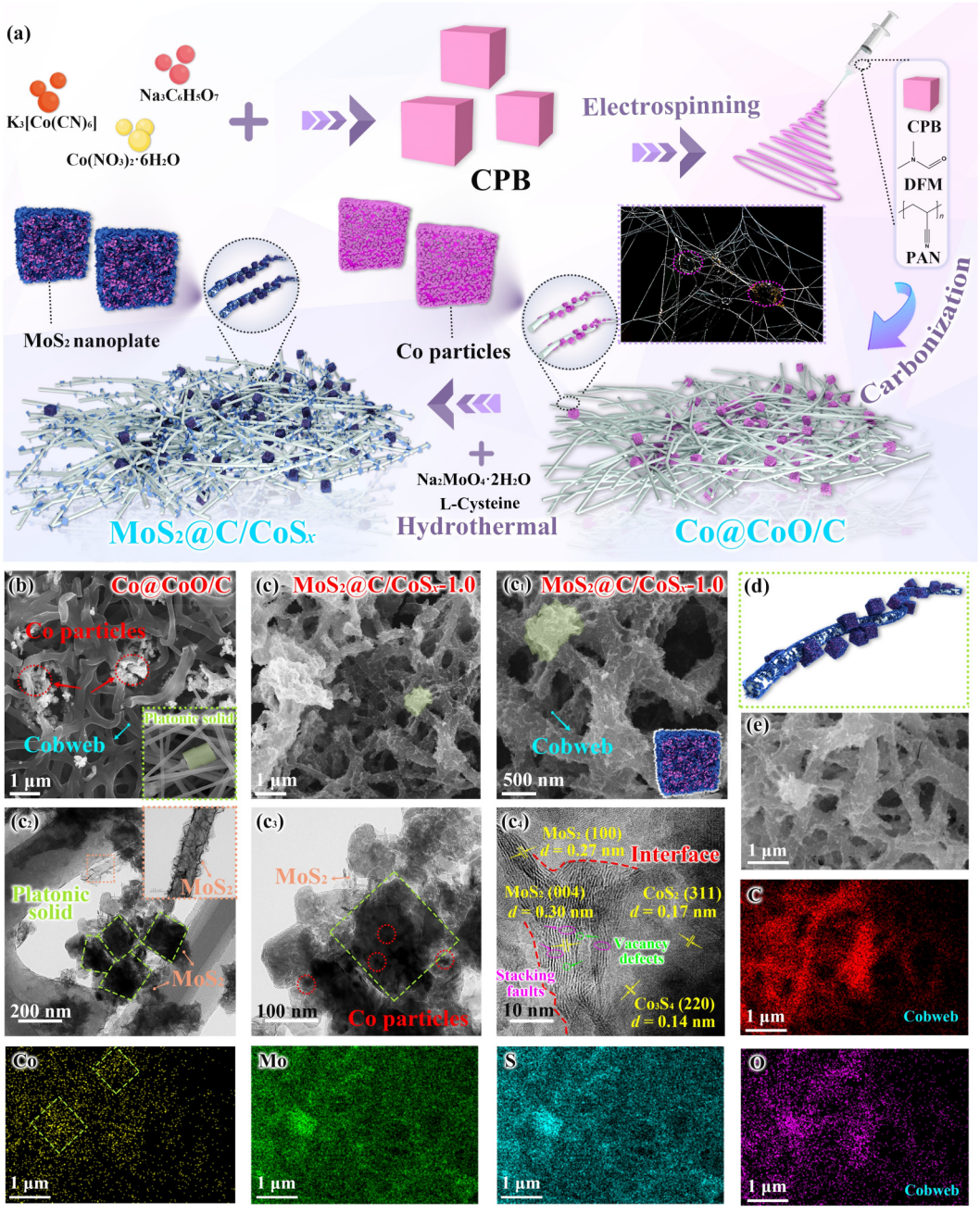

Figure 1 (a) Schematic diagram of preparation process of Co@CoO/C and MoS_2@C/CoS_x. (b)–(c_1) SEM images of Co@CoO/C and MoS_2@C/CoS_x-1.0. (c_2)–(c_4) TEM images, (d) modelling chart, and (e) EDS elemental mapping of MoS_2@C/CoS_x-1.0.

(Figs. 1(c) and 1(c_1)), revealing that the composite retained the biomimetic spiderweb-like structure nanofiber morphology formed during carbonization. Also, the Co nanoparticles and carbon nanofibers were tightly encapsulated by needle-like MoS_2/CoS_x structures, leading to the formation of well-defined heterogeneous interfaces (Fig.1(d)). TEM images (Figs. 1(c_2)–1(c_4)) further revealed structural details. The original CPB particles are transformed into Co particles while preserving their platonic solid morphology (Figs. 1(c_2) and 1(c_3)). The inset of Fig. 1(c_2) clearly displays the typical layered structure of MoS_2. In the high-magnification TEM image (Fig. 1(c_4)), distinct lattice spacings (d) of 0.30 and 0.27 nm are identified, corresponding to MoS_2, along with bent and distorted lattice fringes indicative of edge defects, stacking faults, and point defects. Additional spacings of 0.17 and 0.14 nm are observed, attributed to CoS_2 and Co_3S_4 respectively, confirming the coexistence of multiple CoS_x phases in agreement with XRD analysis. Clear and well-defined interfaces are observed between MoS_2, CoS_2 and Co_3S_4 components. As illustrated by the EDS elemental mapping (Fig. 1(e) and Fig. S3 in the ESM), C and O elements exhibit a typical biomimetic spiderweb-like distribution, while Mo and S elements showed highly overlapping regions, indicating that MoS_2 uniformly coated the surface of the Co@CoO/C framework.

To further elucidate the phase composition of the Co@CoO/C and MoS_2@C/CoS_x composites, X-ray diffraction (XRD) analysis is conducted. According to Fig. 2(a), the diffraction peak observed at

2θ = 24° corresponds to the (002) plane of graphitic carbon, confirming the presence of an ordered graphitized carbon structure within the material [25]. For the Co@CoO/C sample, distinct reflection at 2θ = 36.6°, 42.5° and 61.7° are assigned to the (111), (200) and (220) planes of CoO (PDF #75-0533), implying the successful formation of CoO within the composite [26]. In the MoS_2@C/CoS_x composites, characteristic diffraction peaks at 2θ = 14.3°, 32.9°, 33.6° and 39.8° are ascribed to the (002), (100), (101) and (103) planes of MoS_2 (PDF #73-1508), confirming the incorporation of layered MoS_2 structures. The characteristic peaks at 32.87° and 33.6° reveal the coexistence of 1T and 2H phases in the MoS_2@C/CoS_x composites [27], which corroborates well with the XPS analysis. Additionally, peaks observed at 2θ = 32.2°, 39.8°, 54.9° and 57.6° correspond to the (200), (211), (311) and (222) planes of CoS_2 (PDF #41-1407), while peaks at 2θ = 26.8°, 31.8°, 38.2° and 55.1° are attributed to the (220), (311), and (400) planes of Co_3S_4 (PDF #47-1738). Notably, the overlapping peak at 2θ = 39.8° arises from the superposition of MoS_2 and CoS_2 signals, while the overlapping peak at 2θ = 55.1° results from the superposition of CoS_2 and Co_3S_4. These overlapping peaks indicate the coexistence of Co_3S_4 and CoS_2 in the MoS_2@C/CoS_x composites, leading to the formation of a multiphase cobalt sulfide structure (CoS_x). The formation of such CoS_x structures is likely induced by sulfur vacancies or structural defects introduced during the sulfurization process, which destabilize the single-phase CoS_x lattice and promote heterogeneous phase formation [28]. As a result, structural defects lead to charge accumulation and the formation of polarization centers, which not only enhance dielectric and polarization losses but also improve impedance matching, thereby strengthening the conversion of electromagnetic energy into thermal energy.

The surface chemical composition of the C@CoO/C and MoS_2@C/CoS_x composites is investigated using X-ray photoelectron spectroscopy (XPS). The survey spectra (Fig. 2(b)) confirmed the presence of Co, Mo, S, C and O elements in all composites. High-resolution C 1s and O 1s spectra are shown in Figs. S5(a) and S5(b) in the ESM. In the high-resolution Co 2p spectra (Fig. 2(c) and Fig. S5(c) in the ESM), two typical spin-orbit doublets are observed. The peaks at 779.1 (Co $2p_{3/2}$) and 794.1 eV (Co $2p_{1/2}$) are attributed to Co^{3+}, while those at 780.9 (Co $2p_{3/2}$) and 796.5 eV (Co $2p_{1/2}$) correspond to Co^{2+}. Additionally, two Co^{4+} peaks are observed at 786.2 and 803.7 eV, further confirming the presence of cobalt species. The high-resolution Mo 3d spectrum (Fig. 2(d)) exhibits two characteristic peaks at 228.6 and 229.7 eV, with the former and the latter assigned to Mo $3d_{3/2}$ and Mo $3d_5/_2$ of Mo^{4+}. Importantly, the higher binding energy components can be ascribed to the 1T phase of MoS_2, while the lower ones are associated with the 2H phase [29]. In addition, the peak at 235.8 eV is assigned to the Mo–O bond of oxidized Mo^{6+} species, which likely arises from partial surface oxidation in air, leading to the formation of MoO_x [30]. The peaks at 225.7 and 226.9 eV are attributable to the S 2s spectrum (S–Mo and S–Co) [31]. The S 2p spectrum (Fig. 2(e)) possesses peaks at 161.7 and 162.8 eV, assigned to the S $2p_{3/2}$ and S $2p_{1/2}$ of S–Co bonds in CoS_x, while the peaks at 161.5 and 163.7 eV are attributed to the S $2p_{3/2}$ and S $2p_{1/2}$ of Mo–S bonds

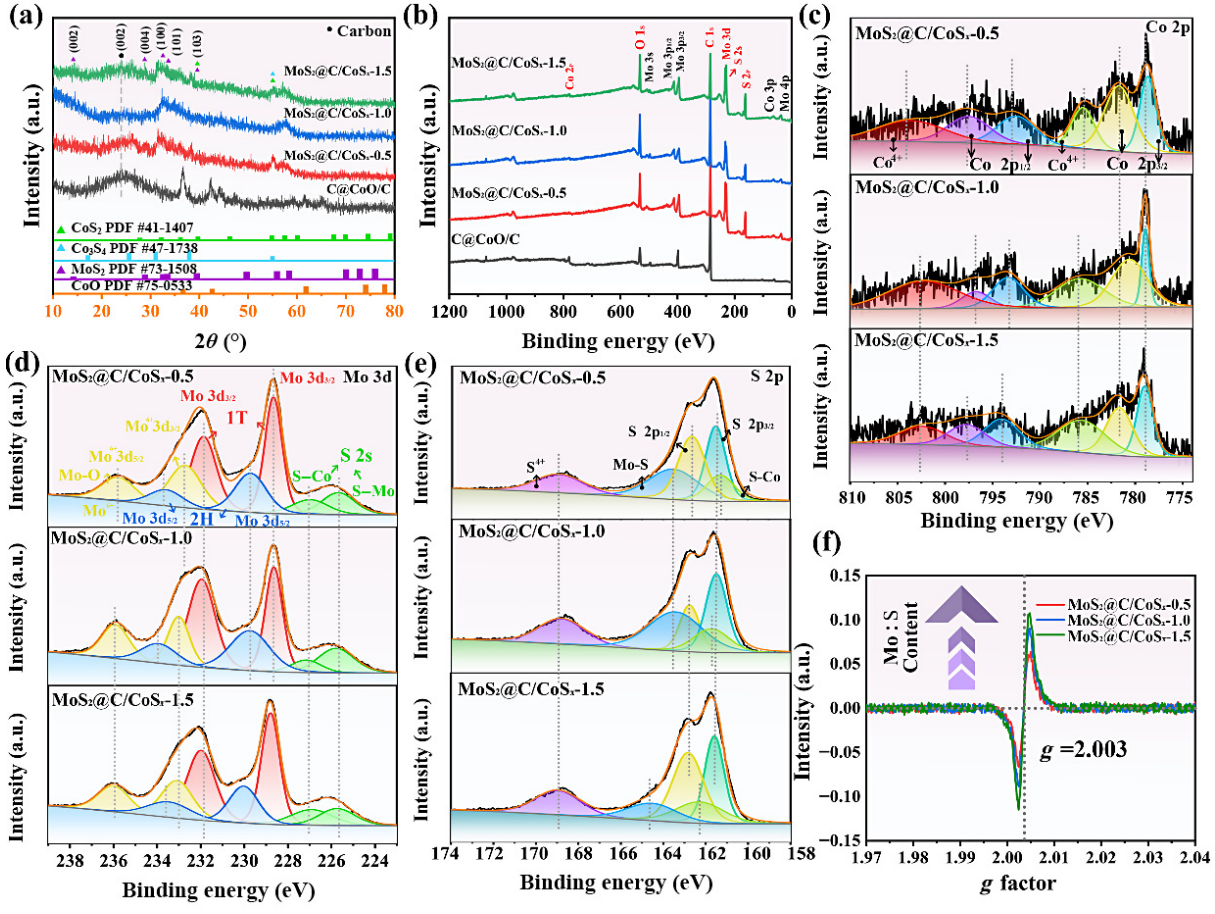

Figure 2 (a) XRD patterns of Co@CoO/C and MoS_2@C/CoS_x composites. (b) XPS survey spectra, (c) Co 2p XPS high-resolution spectra, (d) Mo 2d XPS high-resolution spectra, (e) S 2p XPS high-resolution spectra, and (f) EPR spectra of MoS_2@C/CoS_x composites.

in MoS_2 [32]. Furthermore, the atomic percentage ratios for each state in the MoS_2@C/CoS_x composites are listed in Table S1 in the ESM. These results confirm the successful incorporation of both CoS_x and MoS_2 components in the composite materials.

Electron paramagnetic resonance (EPR) spectra of the MoS_2@C/CoS_x composites (Fig. 2(f)) presents a symmetric signal centered at g = 2.003, which is typically associated with sulfur vacancies and indicates the presence of abundant surface defects and unpaired electrons in the material [33]. The formation of these defects is caused by the anion-exchange reactions occurring during the sulfidation process. Such reactions readily induce lattice distortions and sulfur vacancies, which significantly alter the electronic structure of the MoS_2@C/CoS_x composites and facilitate the construction of the dual-interface BIEF. This observation is consistent with the defect-related features identified in the Raman spectra, further confirming the presence of structural defects within the MoS_2@C/CoS_x composites material.

Raman spectroscopy analysis reveals (Fig. S5(d) in the ESM) that the degree of graphitization of the materials is evaluated by the intensity ratio of the D and G bands (I_D/I_G). Compared with the C@CoO/C, the I_D/I_G ratio of the MoS_2@C/CoS_x composites gradually decreased from 0.847 to 0.840, signifying a reduced degree of carbon disorder and a decline in lattice defects and vacancy concentrations with increasing sodium molybdate dihydrate content. Remarkably, MoS_2@C/CoS_x-1.0 exhibited the lowest I_D/I_G value, suggesting a higher density of lattice distortions and defect sites, consistent with TEM observations, thereby synergistically strengthening the BIEF effect at heterointerfaces. The effective modulation of BIEF plays a pivotal role in boosting polarization loss and overall MA performance.

2.2 Electromagnetic parameters analysis and microwave absorption ability

Matching thickness is a crucial parameter that governs both the absorption efficiency and practical application of MAMs. Based on transmission line theory, the RL_{min} and EAB_{max} of Co@CoO/C and MoS_2@C/CoS_x composites are evaluated across a low thickness range (1–5 mm), as presented in Figs. 3(a_1)–3(c_3). Compared with Co@CoO/C, which exhibits a limited EAB of 1.08 GHz at a 5.0 mm thickness (Fig. S6 in the ESM), the MoS_2@C/CoS_x-1.0 composite delivers a significantly broaden absorption bandwidth of 6.96 GHz at just 2.44 mm thickness. These MoS_2/CoS_2 and CoS_2/C two-electron directional migrations act synergistically to induce the generation of dual-interface BIEF and the formation of an electronically closed loop, which exacerbates the dipole polarization and interfacial relaxation processes. Additionally, MoS_2@C/CoS_x-0.5 and MoS_2@C/CoS_x-1.5 show strong absorption in the frequency ranges of 12.92–17.40 and 10.96–16.20 GHz, respectively, at a thickness of only 1.84 mm (Figs. 3(a_1) and 3(c_1)). More importantly, the introduction of a sulfurized ordered array especially enhances the absorption intensity. A remarkable RL_{min} of –63.83 dB is achieved by MoS_2@C/CoS_x-1.0 at 2.44 mm (Figs. 3(a_2)–3(c_2) and Fig. S7 in the ESM), validating the significant impact of the sulfurization strategy on EMW attenuation capability.

The 2D contour plots of EAB_{max} (Figs. 3(a_3)–3(c_3)) reveal the presence of multiple strong absorption zones across various frequency bands, reflecting a robust thickness-dependent MA response. This offers a rational basis for designing thickness-tunable devices targeting C (4–8 GHz), X (8–12 GHz) and Ku (12–18 GHz) bands. The MoS_2@C/CoS_x-1.0 achieves complete absorption (100%) in the X-Ku band at thicknesses ranging from 1.84 to 3.04 mm (Fig. 3(b_3)). Furthermore, to address absorption issues at lower frequencies (C band), MoS_2@C/CoS_x-0.5 and MoS_2@C/CoS_x-1.0 achieve over 50% effective coverage of the C band at 4.24 and 3.64 mm, respectively. Among these, MoS_2@C/CoS_x-1.5 achieves 75% C band coverage at a thickness of 3.22 mm. This enhanced low-frequency and mid-frequency performance is attributed to intensified polarization relaxation processes, which are promoted by the presence of multi-interfaces and dual-interface BIEF. These findings highlight the critical contribution of interfacial polarization and dipolar loss mechanisms to total EMW attenuation.

Collectively, these results demonstrate that efficient, multiband and tunable MA can be achieved through simple thickness optimization. As presented in Fig. 3(d) and 3(e), the continuous increase in Mo precursor concentration further promotes MA performance, owing to the formation of more robust MoS_2 crystal structure and intensified dual-interface BIEF effects. This is attributed to the synergistic regulation by Mo content, high-defect carbon frameworks and lattice distortion, which collectively influence the RL, EAB and matching thickness. These findings validate the effectiveness of the sulfurized ordered-array strategy in enhancing dielectric loss via dual-interface BIEF construction, offering a promising approach toward the development of broadband, tunable, and high-efficiency MAMs.

The influence of dual-interface BIEF on the electromagnetic response of MoS_2@C/CoS_x composites is further elucidated by analyzing their complex permittivity ($\varepsilon_r = \varepsilon' - j\varepsilon''$) and permeability ($\mu_r = \mu' - j\mu''$) behaviors [34, 35]. As illustrated in Fig. 4(a), the MoS_2@C/CoS_x composites benefits from an ordered array structure formed during the sulfidation process. Compared to the biomimetic spiderweb-like structure of C@CoO/C, this ordered architecture leads to a significant enhancement in both the real part (ε') and the imaginary part (ε'') of the complex permittivity. This enhanced dielectric response demonstrates that the ordered architecture both promotes more efficient charge transport and provides abundant polarization sites, thereby boosting the MA performance. Nevertheless, in comparison with the C@CoO/C, the MoS_2@C/CoS_x composites does not exhibit a significant enhancement in μ_r (Fig. 4(b)). Within the 2–18 GHz frequency range, multiple resonance peaks arise from the combined effects of natural resonance, exchange resonance and eddy current loss mechanisms [36]. Figure 4(c) compares the dielectric loss tangent ($\tan\delta_e = \varepsilon'/\varepsilon''$) and magnetic loss tangent ($\tan\delta_m = \mu'/\mu''$), revealing that dielectric loss predominantly governs the attenuation mechanism of the composite. With the gradual formation of the ordered sulfide array structure, the $\tan\delta_e$ value continuously increases, further confirming that sulfidation enhances dielectric loss by constructing heterogeneous ordered interfaces.

Polarization relaxation, a key dielectric loss mechanism (Fig. 4(d)), is further analyzed through the construction of Cole–Cole plots (Fig. 4(e) and Figs. S8(a)–S8(c) in the ESM). For the MoS_2@C/CoS_x-1.0 material, multiple irregular semicircles and straight tails are observed in the mid-to-high frequency range, indicating the presence of various relaxation processes associated with abundant structural defects, vacancies and lattice distortions. Particularly, the relatively small of the straight tail for MoS_2@C/CoS_x-1.0 suggests that this response is primarily related to conduction loss. It is generally acknowledged that defects and functional groups contribute mainly to low-frequency polarization, whereas interfacial polarization dominates at higher frequencies

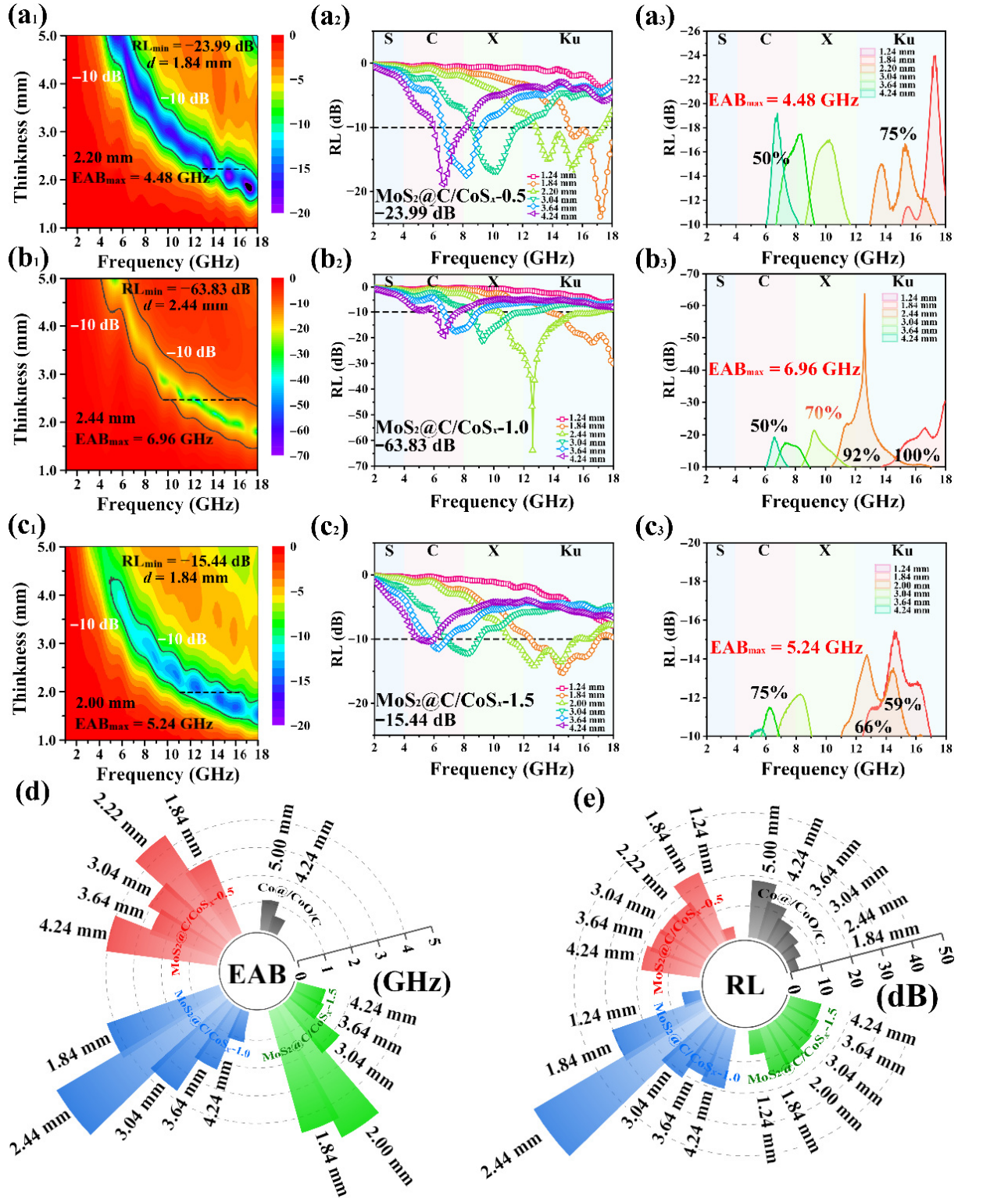

Figure 3 (a_1)–(c_1) 2D color EAB_{max} mappings, (a_2)–(c_2) RL_{min} plots, (a_3)–(c_3) 2D EAB_{max} plots in different frequency bands of MoS_2@C/CoS_x composites at 1–5 mm thickness. (d) RL_{min} values and (e) EAB_{max} values of all composites.

[37]. These results underscore the critical role of interfacial polarization in the MoS_2@C/CoS_x composites. Furthermore, the sulfidation process induces notable microstructural transformations. The carbonized CPB blocks shrink considerably, reducing the encapsulation degree of Co particles and enabling the formation of abundant heterogeneous interfaces. Meanwhile, sulfidation-induced lattice distortions promote enhanced electron hopping and migration within the spiderweb-like network, collectively contributing to stronger polarization responses.

To further elucidate the dielectric relaxation mechanism, the ε'–ε''/f correlation is analyzed (Fig. S9 in the ESM) [38]. The observed linear relationship further supports the dominance of

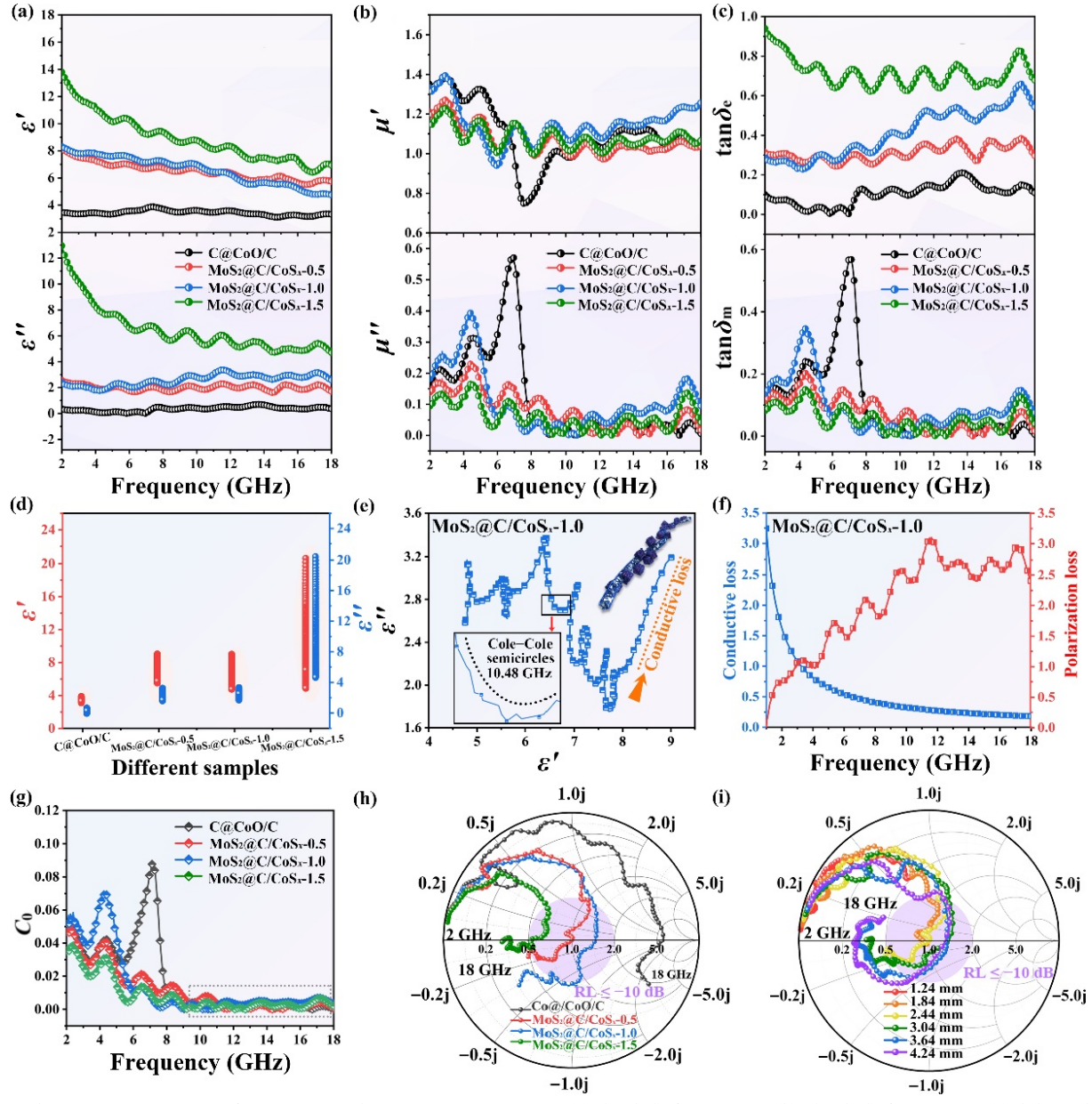

Figure 4 Electromagnetic properties of Co@CoO/C and MoS_2@C/CoS_x composites. (a) ε' and ε'' of permittivity, (b) μ' and μ'' of permittivity, (c) dielectric loss and magnetic loss, (d) complex dielectric constant (real red and imaginary blue), (e) Cole–Cole plots of MoS_2@C/CoS_x-1.0, (f) polarization percentage of MoS_2@C/CoS_x-1.0, (g) Eddy current loss coefficient C_0, (h) impedance matched Smith charts of all samples at 2.44 mm, and (i) impedance matched Smith charts of MoS_2@C/CoS_x-1.0 with 1–5 mm.

dielectric relaxation, as indicated by the variations in slopes in Figs. S9(b)–S9(e) in the ESM. Furthermore, the conduction loss (ε_c'') and polarization loss (ε_p'') are calculated via nonlinear least-squares fitting to distinguish their respective contributions (Fig. 4(f) and Fig. S8(d)–S8(f) in the ESM). As shown in Fig. 4(f), ε_c'' and ε_p'' of the MoS_2@C/CoS_x-1.0 sample are relatively close, yet ε_p'' is clearly higher than ε_c'' within the 4–18 GHz range. This observation is consistent with the Cole–Cole plots presented in Fig. 4(e). These results confirm that the sulfidation-induced ordered array effectively amplifies the dielectric polarization pathways and intensifies polarization strength, thereby enabling precise tuning of dielectric properties.

In terms of magnetic loss mechanisms, the MoS_2@C/CoS_x composites exhibit a transition from natural resonance at low frequencies to eddy current-dominated loss at high frequencies (Fig. 4(f)). The fluctuation of the eddy current coefficient (C_0) in the 2–8 GHz region supports this transition [39]. Meanwhile, the attenuation constant (α), in Fig. S10 in the ESM increases with frequency, with MoS_2@C/CoS_x-1.5 exhibiting the highest α values, attributed to intensified conductive and polarization losses facilitated by BIEF across multi-interfaces.

The impedance matching behavior further highlights the impact of dual-interface BIEF on MA performance. As presented in Figs. 4(h) and 4(i), when the input impedance (Z_{in}) falls within the purple matching circle in the Smith chart, it indicates effective MA with RL ≤ −10 dB. In the low-frequency region, Z_{in} displays an inductive characteristic, which gradually shifts to capacitive behavior as the frequency increases, consistent with observations

[40]. The relatively high dielectric constant of the Co@CoO/C sample causes a marked deviation of its Z_{in} trajectory from the matching circle, suggesting suboptimal impedance matching. Sulfurization serves to effectively reduce the dielectric constant of Co@CoO/C, thereby enhancing its impedance matching capability. As a result, more Z_{in} points fall within the matching circle, corresponding to a broader effective absorption bandwidth. However, with increasing Mo precursor content, the dielectric constant of the MoS_2@C/CoS_x-1.5 composite increases, which significantly enhances conduction loss. This increase leads to greater reflection of incidental EMW at the material surface, driving the Z_{in} trajectory further away from the matching region and ultimately deteriorating the impedance matching and absorption performance. Furthermore, Fig. 4(i) reveals that the Z_{in} points of the MoS_2@C/CoS_x-1.0 composite at a thickness of 2.44 mm are most densely distributed within the purple circle, suggesting that this thickness condition achieves the best impedance matching and thus the most favorable MA performance.

Additionally, Fig. S11 in the ESM illustrates the relationship between thickness, frequency, and impedance matching ($|Z_{in}/Z_0|$) values. The MoS_2@C/CoS_x-1.0 composite displays the widest impedance matching window, marked by the largest green region near the ideal matching line ($|Z_{in}/Z_0| = 1$), underscoring the optimal balance between permittivity and permeability achieved through dual-interface BIEF construction. These observations align well with Smith chart results and further validate that the dual-interface strategy not only enhances polarization strength but also enables precise impedance regulation over a broad frequency range.

2.3 Constructing dual-interface BIEF heterointerfaces and MA mechanism

Figure 5 presents a theoretical elucidation of how dual-interface BIEF regulate the EMW attenuation mechanism of MoS_2@C/CoS_x composites, based on density functional theory (DFT) calculations. To reveal the underlying interfacial charge dynamics, the work function, Fermi level, differential charge density and density of

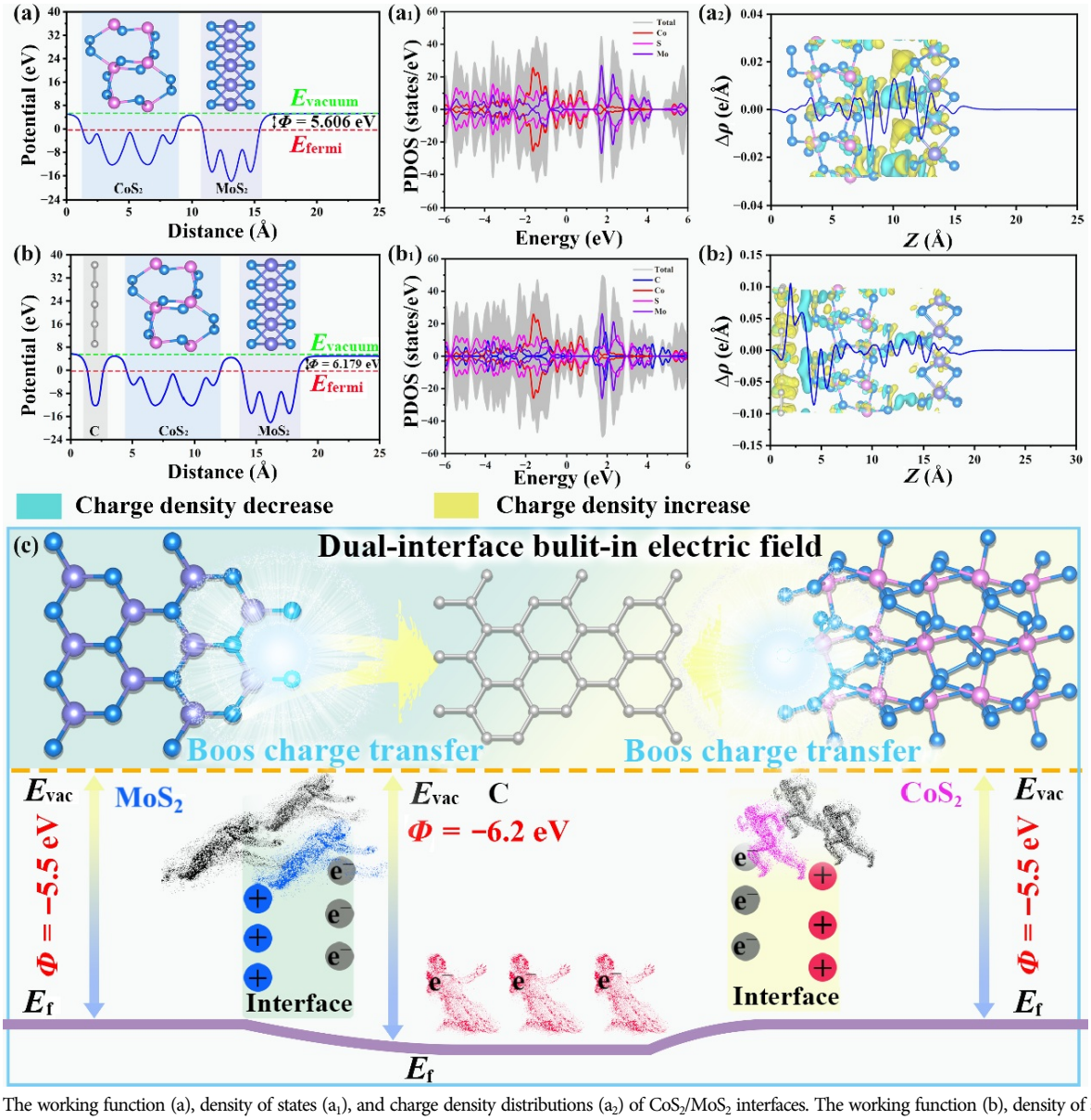

Figure 5 The working function (a), density of states (a_1), and charge density distributions (a_2) of CoS_2/MoS_2 interfaces. The working function (b), density of states (b_1), and charge density distributions (b_2) of C/CoS_2/MoS_2 interface. (c) Dual-interface BIEF heterointerfaces model.

states (DOS) of representative heterointerfaces (CoS_2/MoS_2 and $C/CoS_2/MoS_2$) are systematically analyzed. The work function reflects the minimum energy needed for electrons to escape from the Fermi level into vacuum and variations in $\Delta\Phi$ between adjacent components drive interfacial charge redistribution [41]. Differential charge density maps visualize the redistribution of electrons at the interface, where yellow and green regions indicate charge accumulation and depletion [42].

For the CoS_2/MoS_2 and $C/CoS_2/MoS_2$ interfaces, the calculated work functions are 5.606 and 6.179 eV, respectively (Figs. 5(a) and 5(b)). The difference in work function drives the spontaneous formation of BIEF. The higher work function at the $C/CoS_2/MoS_2$ interface suggests a stronger driving force for electron migration from CoS_2/MoS_2 toward the C layer, leading to the development of a dual-interface BIEF. This built-in potential facilitates interfacial charge migration, promotes interface polarization and enhances polarization loss.

The DOS results (Figs. 5(a_1) and 5(b_1)) reveal that the density of states near the Fermi level is significantly higher for $C/CoS_2/MoS_2$ compared to CoS_2/MoS_2, mainly due to the contribution from the C matrix. A higher DOS implies enhanced charge carrier mobility and superior dielectric loss ability, suggesting that the incorporation of C not only contributes to conductivity-driven loss, but also amplifies interfacial polarization through electronic coupling at the MoS_2-CoS_2-C junction.

The average charge density difference ($\Delta\rho$) reflects the variation of charge along the direction perpendicular to the interface [43]. As illustrated in Figs. 5(a_2) and 5(b_2), the CoS_2/MoS_2 interface shows weak charge separation (Fig. 5(a_2)), indicating a negligible BIEF effect. In contrast, the $C/CoS_2/MoS_2$ interface reveals clear charge depletion at the CoS_2 surface and charge accumulation on the C layer (Fig. 5(b_2)). This asymmetrical charge redistribution is a signature of a Schottky-type heterojunction formed between metallic C and semiconductive CoS_2/MoS_2, which significantly boosts dipolar polarization intensity.

The work functions of MoS_2, CoS_2 and C are −5.5, −5.5 and −6.2 eV, respectively. This energy alignment favors spontaneous electron transfer from MoS_2 and CoS_2 to the more electronegative C phase, resulting in dual charge-transfer pathways. The synergistic electron migration across both CoS_2/MoS_2 and CoS_2/C interfaces leads to the formation of dual-interface BIEF, as schematically illustrated in Fig. 5(c) [44]. These dual internal fields synergistically couple conduction and polarization losses: while one interface (CoS_2/MoS_2) initiates dipole formation and charge trapping, the other (CoS_2/C) sustains long-range directional transport across the conductive network. Under high-frequency EMW excitation, the dual-interface BIEF triggers rapid, directional polarization relaxation and localized dipole oscillations, thus efficiently dissipating incident energy. This multi-interface coupling mechanism enables simultaneous optimization of impedance matching and dielectric loss. Therefore, the construction of dual-interface BIEF heterointerfaces not only amplifies interfacial polarization intensity but also promotes effective EMW attenuation via a dual-pathway polarization-conduction mechanism.

Figure 6 presents the MA mechanism of the MoS_2@C/CoS_x composites. This composite material exhibits abundant heterogeneous interfaces, primarily originating from the double-interface BIEF heterostructure formed between MoS_2, CoS_x and the C phase. This architecture markedly reinforces the interfacial polarization effect and extends the polarization relaxation time, thereby yielding an enhanced dielectric loss. Meanwhile, the biomimetic spiderweb-like structure constructed via electrospinning and carbonization serves as a robust conductive framework, enabling continuous electron transport pathways throughout the network [45]. This architecture promotes both axial electron migration and inter-fiber hopping conduction, which in turn enhances conduction loss under alternating electromagnetic fields. Meanwhile, as a result, strengthens interfacial polarization and prolongs polarization time, synergistically improving the dielectric loss efficiency. In addition, oxygen-containing functional groups, lattice defects and sulfur vacancies generated during the carbonization and sulfidation processes act as localized dipole centers within the composite. Under the influence of the external electric field, these centers induce dipole polarization and further promoting the dielectric response [46]. Besides, the eddy current loss and exchange resonance effects arising from the magnetic Co

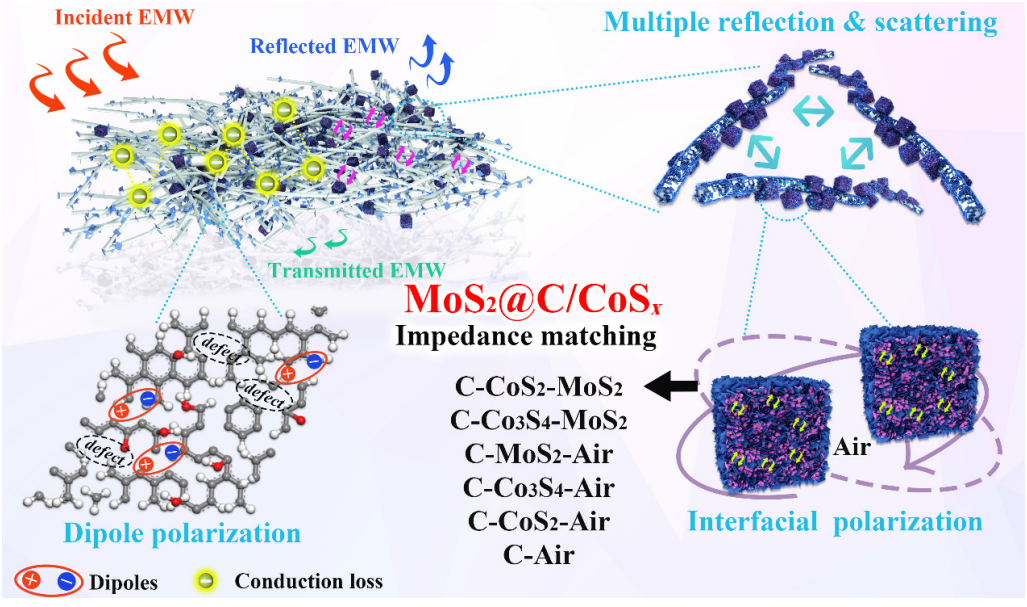

Figure 6 The microwave absorption mechanism of the MoS_2@C/CoS_x samples.

particles complement the dielectric loss mechanism and contribute to improved impedance matching, ultimately enabling broadband and efficient MA performance.

2.4 Thermal insulation capacities

Excellent thermal infrared stealth performance is also of great significance for MAMs, as it can effectively suppress the leakage of infrared radiation signals, thereby ensuring the safe operation of electronic devices in complex thermal environments [47]. To evaluate the thermal management performance of the materials, C@CoO/C and MoS_2@C/CoS_x-1.0 composites are placed on a heating platform maintained at 80 °C for 10 min, and their real-time infrared images and surface temperature profiles are recorded using an infrared thermal imaging device. As shown in Figs. 7(a) and 7(b), MoS_2@C/CoS_x-1.0 exhibits a substantially lower surface temperature than C@CoO/C, with a temperature drop exceeding 45 °C compared to the heating platform. This remarkable thermal insulation behavior is primarily attributed to its unique biomimetic spiderweb-like structure, which creates a tortuous path for phonon conduction and delays heat transfer. Meanwhile, the abundant air voids within the structure further hinder heat flow, thus playing a critical role in maintaining a lower surface temperature [48]. In parallel the infrared thermal image (Fig. 7(c)) further confirms the material's infrared stealth capability. The MoS_2@C/CoS_x-1.0 sample appears uniformly dark in the thermal image and blends well with the surrounding environment, demonstrating excellent thermal camouflage potential and highlighting its application prospects in the field of infrared stealth.

To assess the material's thermal stability, thermogravimetric analysis (TGA) is conducted under an inert argon atmosphere from 100 to 800 °C (Fig. 7(d)). The total weight losses for C@CoO/C, MoS_2@C/CoS_x-0.5, MoS_2@C/CoS_x-1.0, and MoS_2@C/CoS_x-1.5 were 21.22%, 20.1%, 14.6%, and 24.0%, respectively. The biomimetic spiderweb-like structure endows MoS_2@C/CoS_x-1.0 with more than just excellent thermal insulation additionally outstanding infrared stealth and thermal stability, making it a promising candidate for applications in high-temperature or harsh environments.

3 Conclusion

In summary, a dual-functional MoS_2@C/CoS_x composites with dual-interface BIEF at heterogeneous interfaces is successfully fabricated by a combination of electrospinning, thermal treatment and sulfidation strategies. The ordered array architecture inspired by spiderweb-like structures enabled the construction of multiple heterogeneous interfaces and the spontaneous formation of dual-interface BIEF by regulating interfacial work function differences. The presence of dual-interface BIEF induced asymmetric charge redistribution and facilitated directional electron transfer, which enhanced dipolar and interfacial polarization and significantly improved dielectric loss behavior. As a result, the composite achieved an outstanding minimum reflection loss of –63.83 dB and a broad effective absorption bandwidth of 6.96 GHz, with full-band absorption performance in both C and Ku bands at various thicknesses (1.84–3.04 mm). DFT calculations further confirmed the strong internal electric field (~ 6.179 eV) at the C/CoS_2/MoS_2 heterointerface, validating the crucial role of dual-interface BIEF in promoting interfacial polarization and enhancing dielectric response. This study provides a rational design strategy for engineering dual-interface BIEF at heterogeneous interfaces and offers valuable insights into the development of advanced MAMs

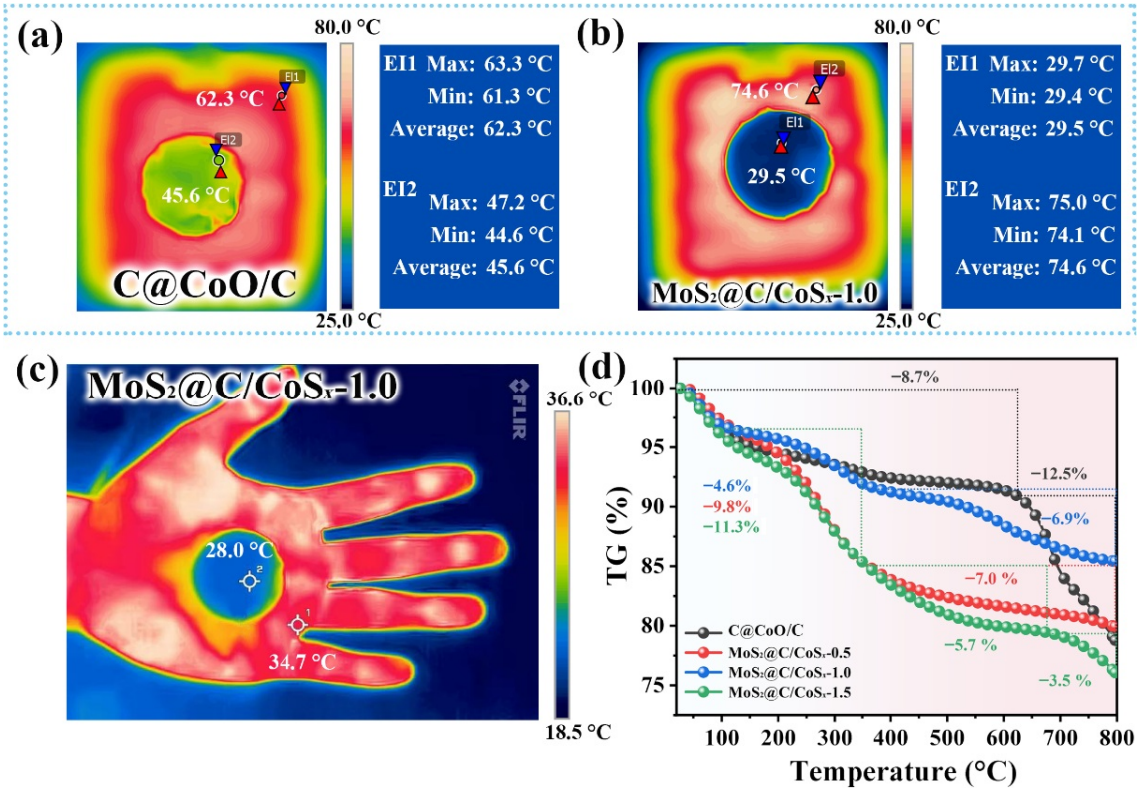

Figure 7 Infrared thermal images of (a) C@CoO/C and (b) MoS_2@C/CoS_x-1.0 taken within 10 min. (c) Infrared thermal image of MoS_2@C/CoS_x-1.0 placed on the hand. (d) TGA curves of C@CoO/C and MoS_2@C/CoS_x composites.

with broadband absorption and thermal camouflage capabilities.

Electronic Supplementary Material: Supplementary material (experimental section and characterization of MoS_2@C/CoS_x samples) is available in the online version of this article at https://doi.org/10.26599/NR.2025.94908070.

Data availability

All data needed to support the conclusions in the paper are presented in the manuscript and the Electronic Supplementary Material. Additional data related to this paper may be requested from the corresponding author upon request.

Acknowledgements

This work was financially supported by the National Natural Science Foundation of China (No. 52462026), Postdoctoral Research Foundation of China (No. 2018M643699), and Shaanxi Province Postdoctoral Science Foundation (No. 2018BSHEDZZ 101).

Author contribution statement

H. W.: Writing – original draft, software, conceptualization, writing – review & editing. J. R. Z: project administration, writing – review & editing. Z. W.: Funding acquisition, project administration, writing – review & editing.

Declaration of competing interests

All the contributing authors report no conflict of interests in this work.

Use of AI statement

None.

References

[1] Chen, Y. Q.; Chen, M.; Lei, H. Y.; Song, L. M.; Zhang, R.; Li, H. X.; Tian, M.; Fan, B. B. Microwave-assisted synthesis of high-performance TaC nanorods for enhanced electromagnetic wave absorption. *J. Adv. Ceram.* **2025**, *14*, 9221130.

[2] Li, M. R.; Li, W.; Wang, Y. X.; Sun, F.; Wang, Q.; Tan, D. L.; Zhang, R.; Wang, H. L.; Shao, G.; Liu, Y. L. et al. Entropy-driven microwave absorption enhancement in hexagonal $(Ba_{1/3}Sr_{1/3}Ca_{1/3})FeO_3$ perovskite. *J. Adv. Ceram.* **2025**, *14*, 9221059.

[3] Wang, D. S.; Ping, T.; Du, Z. L.; Liao, Y.; Gao, H.; Gong, X. B.; Rao, J. S.; Wang, B.; Wei, S. C.; Liu, X. Y. et al. Multistage carbon coupling on three-dimensional multi-space biological templates: A novel strategy for multifunctional microwave absorption aerogel. *Nano Res.* **2025**, *18*, 94907226.

[4] Lin, Y. T.; Zhou, X.; Wang, Y. R.; Hou, J. H.; Wang, D. M.; Tong, G. X.; Cao, Y. Progress of MOFs composites in the field of microwave absorption. *Carbon* **2025**, *238*, 120241.

[5] Mao, M. Z.; Xia, P. K.; Ma, L.; Huang, S. X.; Gao, X. H.; Deng, L. W. Nitric acid oxidation treatment promoting microwave absorption performance of carbonized melamine foam. *J. Cent. South Univ.* **2025**, *32*, 1630–1640.

[6] Zhang, J. H.; Li, X. N.; Hu, H. J.; Huang, H. W.; Li, H.; Sun, X. D.; Ma, T. Y. Enhancing photocatalytic performance of covalent organic frameworks via ionic polarization. *Nat. Commun.* **2024**, *15*, 9576.

[7] Bao, Y. F.; Wang, W. R.; Liu, Y.; Yue, Z. H.; Guo, S. Y. Self-assembly $Ti_3C_2T_x$ MXene/$ZnCo_2O_4$@ZnO heterostructure with Schottky junction for regulating BIEF to enhance microwave absorption. *Appl. Surf. Sci.* **2025**, *680*, 161393.

[8] Gao, K. W.; Zhou, M.; Liu, Y. F.; Wang, S. C.; Fu, R.; Wang, Z. Y.; Guo, J. H.; Liu, Z. A.; Wang, H. R.; Zhao, Y. et al. The dual built-in electric fields across CoS/MoS_2 heterojunctions for energy-saving hydrogen production coupled with sulfion degradation. *J. Colloid Interface Sci.* **2024**, *657*, 290–299.

[9] Koo, M. C.; Zhang, Y.; Cai, B.; Liang, C. M.; Shi, S. H.; Peng, H. L.; Yang, S. H.; Sun, X. B.; Wang, G. S. Enhancing microwave absorbing properties of C/TiO_2/NiNW composites through built-in electric field effect. *J. Mater. Sci. Technol.* **2026**, *244*, 102–110.

[10] Zhai, N. X.; Wang, Z. H.; Cheng, Z. Z.; Xu, Z. H.; Guo, K. K.; Zhou, W. P.; Gao, F.; Luo, G. S.; Ji, G. B. Simultaneous manipulation of multidimensional heterojunctions and dielectric gene engineering for broadband microwave absorption. *Adv. Funct. Mater.* **2025**, *35*, 2502480.

[11] Liu, Y. L.; Geng, W. Z.; Wang, L. N.; Wang, H. L.; Zhang, R.; Lan, D.; Fan, B. B. Designing MXene hydrogels for flexible and high-efficiency electromagnetic wave absorption using digital light processing 3D printing. *Chem. Eng. J.* **2025**, *505*, 159489.

[12] Pan, J. L.; Zhang, R. J.; Ling, J.; Wang, M.; Li, Z. C.; Zhen, Z.; He, L. M.; Zhu, H. W. Controllable preparation and microwave absorption properties of shape anisotropic Fe_3O_4 nanobelts. *J. Materiomics* **2021**, *7*, 957–966.

[13] Liang, X. H.; Wang, G. H.; Gu, W. H.; Ji, G. B. Prussian blue analogue derived carbon-based composites toward lightweight microwave absorption. *Carbon* **2021**, *177*, 97–106.

[14] Xing, H. L.; You, X. M.; Liu, H.; Wang, Y. Microwave absorption properties of N-doped raspberry-like MWCNT/Fe_2O_3 composites based on Prussian blue. *J. Mater. Sci.: Mater. Electron.* **2023**, *34*, 1427.

[15] Wang, Z. X.; Jia, Z. R.; Ren, J. W.; Wang, L.; Lan, D.; Zhang, S. Y.; Shi, X. T.; Liu, X. H.; Gao, Z. G.; Wu, G. L. Multi-topological network engineering of Co/MnO composites for electromagnetic wave absorption. *J. Mater. Sci. Technol.* **2025**, *235*, 81–90.

[16] Han, L. Y.; Yang, H. B.; Cai, Z. X.; Lin, Y. Construction of flexible magnetic carbon nanofibers by core-shell MOF derivatives for optimizing microwave absorption. *Carbon* **2025**, *232*, 119817.

[17] Jiang, X. W.; Wang, Q.; Song, L. M.; Lu, H. X.; Xu, H. L.; Shao, G.; Wang, H. L.; Zhang, R.; Wang, C. G.; Fan, B. B. Enhancing electromagnetic wave absorption with core-shell structured SiO_2@MXene@MoS_2 nanospheres. *Carbon Energy* **2024**, *6*, e502.

[18] Zhao, J. R.; Wang, H.; Li, Y.; Wang, Z.; Fang, C. Q.; Liu, P. B. Construction of self-assembled bilayer core-shell V_2O_3 microspheres as absorber with superior microwave absorption performance. *J. Colloid Interface Sci.* **2023**, *639*, 68–77.

[19] Wang, H.; Kang, H. T.; Wang, Z.; Zhao, J. R. Waste leaves into biomass carbon materials with tunable oxygen-containing functional groups for microwave absorption. *Carbon* **2025**, *234*, 119930.

[20] Wang, J.; Wu, Z. C.; Yang, C. D.; Chen, G. Y.; Yuan, M. Y.; Li, B. X.; Lai, Y. X.; Che, R. C. Controllable regulation of MoS_2 surface atomic exposure for boosting interfacial polarization and microwave absorption. *Adv. Funct. Mater.* **2024**, *34*, 2409923.

[21] Zhao, J. G.; Nguyen, T. K. Y.; Mehrez, S.; Mohanavel, V.; Fayed, M.; Mahariq, I.; Du, G. Development of ultra-thin and high-efficient bi-layer microwave absorbers from Fe_3N@C and CoS_2 samples. *Ceram. Int.* **2023**, *49*, 14750–14759.

[22] Xu, D. W.; Zhang, F. F.; Guo, H. H.; Liu, S. T.; Ma, S. J.; Guo, X. Q.; Chen, P. Hierarchical dandelion-like CoS_2 hollow microspheres: Self-assembly and controllable microwave absorption performance. *RSC Adv.* **2023**, *13*, 27147–27157.

[23] Zhang, L.; Huo, Y. S.; Liu, Y.; Zhao, M. S.; Tan, Y. J.; Huo, S. Y.; Yao, L.; Qu, S. H.; He, Z. H. Design and synthesis of non-homogeneous CoS_2/carbon composite nanofibers for enhanced microwave absorption. *Carbon* **2025**, *236*, 120120.

[24] Yang, L. F.; Zhang, L.; Xu, G. C.; Ma, X.; Wang, W. W.; Song, H. J.; Jia, D. Z. Metal-organic-framework-derived hollow CoS_x@MoS_2 microcubes as superior bifunctional electrocatalysts for hydrogen evolution and oxygen evolution reactions. *ACS Sustainable Chem. Eng.* **2018**, *6*, 12961–12968.

[25] Wang, Z.; Yang, K. X.; Wang, H.; Zhao, J. R.; Liu, P. B. CNTs decorated Fe_3O_4/Co-Ni polyhedrons with heterogeneous interfaces for promoting microwave absorption. *Compos. Commun.* **2024**, *49*, 101976.

[26] Ding, Z. Z.; Zhao, Z. X.; Zhang, Q. C.; Huang, S. L.; Hassan, Y. A.; Chen, A. L.; Jiang, C.; Du, Z. J. Cobalt oxide/graphene composites with abundant interface types for tunable broadband microwave absorption. *Ceram. Int.* **2025**, *51*, 15204–15214.

[27] Liu, S. Q.; Fang, D. B.; Xing, F. Y.; Jin, H. B.; Li, J. B. Auricularia-shaped MoS_2 nanosheet arrays coated hierarchical multilayer MoS_2/PPy/rGO composites for efficient microwave absorption. *Chem. Eng. J.* **2024**, *479*, 147613.

[28] He, Z. Z.; Shi, L. Z.; Sun, R.; Ding, L. F.; He, M. K.; Li, J. M.; Guo, H.; Gao, T. D.; Liu, P. B. Low-temperature oxidation induced phase evolution with gradient magnetic heterointerfaces for superior electromagnetic wave absorption. *Nano-Micro Lett.* **2025**, *17*, 7.

[29] Baker, M. A.; Gilmore, R.; Lenardi, C.; Gissler, W. XPS investigation of preferential sputtering of S from MoS_2 and determination of MoS_x stoichiometry from Mo and S peak positions. *Appl. Surf. Sci.* **1999**, *150*, 255–262.

[30] Zhao, J. R.; Wang, Z.; Wang, H.; Liu, P. B.; Che, R. C. Controllable design of "nested doll" MoS_2/V_2O_3 heterostructures promotes polarization effects for high-efficiency microwave absorption. *Adv. Funct. Mater.* **2025**, *35*, 2418282.

[31] Yang, Y.; Wang, Y. T.; He, H. L.; Yan, W. J.; Fang, L.; Zhang, Y. B.; Qin, Y.; Long, R.; Zhang, X. M.; Fan, X. J. Covalently connected $Nb_4N_{5-x}O_x$-MoS_2 heterocatalysts with desired electron density to boost hydrogen evolution. *ACS Nano* **2020**, *14*, 4925–4937.

[32] Chu, F. Y.; Jiang, H. L.; Li, X. C.; Wang, X. R.; He, G. H.; Ruan, X. H. MnO/MnS-based dual built-in electric fields constructed in N-doped carbon armors to regulate p-band center and promote reaction kinetics in Li-S batteries. *Chem. Eng. J.* **2025**, *519*, 165275.

[33] Zhao, J. R.; Wang, Z.; Wang, H. W.; Cheng, X. Y.; Yan, C.; Liu, P. B. Fish Tofu-structured Se/prussian blue derived composites for exceptional microwave absorption. *Mater. Today Nano* **2025**, *29*, 100585.

[34] Song, L. M.; Hu, F. Y.; Chen, Y. Q.; Guan, L.; Zhang, P. G.; Wang, L. N.; Sun, Z. M.; Zhu, Y. Q.; Wang, H. L.; Che, R. C. et al. Heterointerface-engineered SiC@SiO_2@C nanofibers for simultaneous microwave absorption and corrosion resistance. *Adv. Sci.* **2025**, e09071.

[35] Song, L. M.; Wang, L. N.; Chen, Y. Q.; Wu, H. J.; Song, B. Z.; Wang, N. N.; Guan, L.; Wang, H. L.; Zhang, R.; Zhu, Y. Q. et al. Engineered core-shell SiC@SiO_2 nanofibers for enhanced electromagnetic wave absorption performance. *Small* **2024**, *20*, 2407563.

[36] Liu, J. L.; Zhang, S. Y.; Qu, D.; Zhou, X. J.; Yin, M. X.; Wang, C. X.; Zhang, X. L.; Li, S. C.; Zhang, P. J.; Zhou, Y. Q. et al. Defects-rich heterostructures trigger strong polarization coupling in sulfides/carbon composites with robust electromagnetic wave absorption. *Nano-Micro Lett.* **2025**, *17*, 24.

[37] Zeng, X. J.; Jiang, X.; Ning, Y.; Gao, Y. F.; Che, R. C. Constructing built-in electric fields with semiconductor junctions and schottky junctions based on Mo-MXene/Mo-metal sulfides for electromagnetic response. *Nano-Micro Lett.* **2024**, *16*, 213.

[38] Gao, Z. G.; Iqbal, A.; Hassan, T.; Hui, S. C.; Wu, H. J.; Koo, C. M. Tailoring Built-in electric field in a self-assembled zeolitic imidazolate framework/MXene nanocomposites for microwave absorption. *Adv. Mater.* **2024**, *36*, 2311411.

[39] Huang, J.; Zeng, X. J.; Jiang, X.; Deng, X. M.; Wu, Z. M.; Gao, Y. F. *In situ* construction of MXene derivatives and rare metal doping in nanofibers for multifunctional and ultrathin electromagnetic responses. *Adv. Funct. Mater.* **2025**, e10047.

[40] Wang, D. S.; Hu, Y. Z.; Cui, Z. Y.; Yang, P. X.; Du, Z. L.; Hou, Y.; Yang, P. G.; Rao, J. S.; Wang, C.; Zhang, Y. X. Sulfur vacancy regulation and multipolarization of Ni_xCo_1S nanowires-decorated biotemplated structures to promote microwave absorption. *J. Colloid Interface Sci.* **2023**, *646*, 991–1001.

[41] Jeong, G.; Frisbie, C. D. Molecular tunnel junctions based on mixed SAMs: Exponential correlation of the average metal-HOMO coupling with SAM/metal work function. *Nanoscale* **2025**, *17*, 8912–8922.

[42] Wang, H.; Zhao, J. R.; Wang, Z.; Shi, Z. H.; Li, N. Construction of ZIF-67 derived multi-interfacial composites embedded in carbonized pomelo peel for enhanced microwave absorption with 8 wt% filler loading. *J. Alloy. Compd.* **2024**, *985*, 174124.

[43] Feuer, M. L.; Thinel, M.; Huang, X.; Cui, Z. H.; Shao, Y. M.; Kundu, A. K.; Chica, D. G.; Han, M. G.; Pokratath, R.; Telford, E. J. et al. Charge density wave and ferromagnetism in intercalated CrSBr. *Adv. Mater.* **2025**, *37*, 2418066.

[44] Lin, J.; Wen, H. L.; Feng, Z. B.; Hu, R. Z.; Wu, L. P.; Liu, C. B.; Lin, S.; Peng, Y. H.; Liu, Y. F.; Che, R. C. Anion injection in dielectric ecosystems to construct dual built-in electric fields for efficient electromagnetic response. *Adv. Funct. Mater.* **2025**, 2505381.

[45] Wang, D. S.; Yang, P. X.; Hu, Y. Z.; Cui, Z. Y.; Du, Z. L.; Yang, P. G.; Yi, S.; Rao, J. S.; Zhang, Y. X. 1D-3D biological template loaded NiCo nanowires at high temperatures as a broadband, lightweight electromagnetic wave absorbing material. *Powder Technol.* **2023**, *426*, 118670.

[46] Wang, D. S.; Ping, T.; Du, Z. L.; Liu, X. Y.; Zhang, Y. X. Lessons from nature: Advances and perspectives in bionic microwave absorption materials. *Nano-Micro Lett.* **2025**, *17*, 100.

[47] Wang, H. Y.; Yang, W. T.; He, Z. M.; Huang, Y. J.; Wang, G. S.; Zhu, Y. F. Construction of a partially rGO multifunctional aerogel with multi-stage pores for hydrophobicity, thermal insulation and efficient microwave absorption property. *J. Mater. Chem. C* **2025**, *13*, 13672–13682.

[48] Wang, X. X.; Wang, C.; Wang, Y. J.; You, G. M.; Gu, X. K.; Chen, J.; Jin, Y. L.; Peng, C. X.; Yan, Y. L.; Zheng, H. W. et al. High thermoelectric performance in n-type PbSe achieved through thermal mismatch inducing porous structure and lattice plainification. *Nano Energy* **2025**, *142*, 111126.